Journal of Stress Analysis
Vol. 9, No. 1, 2025, 51-65
Bu-Ali Sina University

ORIGINAL RESEARCH PAPER

# Hygro-Thermo-Elastic Creep Analysis of a Rotating Variable Thickness Multi-Layered Functionally Graded Disc with Weak Interlayer Bonding

**Mahdi Saadatfar***, **Yousef Iravani, Mohammad Amin Babazadeh**
Department of Mechanical Engineering, University of Qom, Qom, Iran.

## Article info

*Article history:*
Received 15 March 2025
Received in revised form
05 May 2025
Accepted 28 June 2025

*Keywords:*
Functionally graded material
Creep response
Rotating disc
Variable thickness
Hygrothermal

**Abstract**

This article studies the time-dependent creep response of a rotating multi-layered functionally graded disc with variable thickness and weak interlayer bonding, subjected to axisymmetric thermal and moisture fields and a constant magnetic field. The disk thickness and material coefficients are power functions dependent on the radius. Based on the constitutive stress–strain relations, the equilibrium formulation was developed to account for creep terms, and by initially eliminating the creep strain, the primitive stress and displacement fields were obtained analytically. Using Prandtl–Reuss relations for creep modeling, a complete analytical solution was formulated, and the rates of various parameters were evaluated. Lastly, an iterative technique was employed to track the time evolution of various field variables. The governing equations for the static state were analytically solved to determine the initial values at zero time. Also, the creep evolution equations were solved analytically to obtain the corresponding rate of fields. Subsequently, first the initial response was established, and then the time-dependent behavior at successive intervals was computed iteratively based on the evaluated rate of fields. The results highlight the significant influence of the grading index, imperfect bonding, angular velocity, hygrothermal loading, and magnetic field on the disc's response.

## Nomenclature

| | | | |
|---|---|---|---|
| $r_o$ | Outer radius (m) | $\sigma_r$ | Radial stress (Pa) |
| $r_i$ | Inner radius (m) | $\sigma_\theta$ | Hoop stress (Pa) |
| $H_z$ | Magnetic field | $\sigma_e$ | Von-Mises equivalent stress (Pa) |
| $T$ | Temperature (K) | $u_r$ | Radial Displacement (m) |
| M | Moisture concentration | $\omega$ | Rotational-angular speed (Rad/s) |
| $f_r$ | Lorentz force (N) | $c_{ij}$ | Elastic constants (GPa) |
| $\lambda_i$ | Thermal modulus ($N/m^2K$) | $\alpha_i$ | Thermal expansion coefficients (1/K) |
| $\zeta_i$ | moisture modulus | $\beta_i$ | Moisture expansion coefficients |
| $\gamma$ | Grading index | $\rho$ | Density ($Kg/m^3$) |
| $dt$ | Time increment (s) | $\varepsilon_i$ | Components of strain |
| $\mu$ | Magnetic permeability ($N/A^2$) | A | Imperfection coefficient |
| $h(r)$ | Thickness function | $\varepsilon_i^c$ | Components of creep strain |

*Corresponding author: M. Saadatfar (Associate Professor)
E-mail address: m.saadatfar@gmail.com
10.22084/JRSTAN.2025.30984.1268
ISSN: 2588-2597

| | | | |
|---|---|---|---|
| $\Omega$ | Thickness profile coefficient | $\dot{\varepsilon}_c^i$ | Components of creep strain rate (1/s) |
| $y_0$ | Thickness profile coefficient | $\dot{\varepsilon}_e^i$ | Effective creep strain rate (1/s) |
| $\chi_i^T$ | Thermal compliance coefficient (K.m$^2$/W) | $\chi_i^M$ | Moisture compliance coefficient (m.s) |

## 1. Introduction

ndent Functionally graded materials (FGMs) are an advanced class of composites that have attracted significant interest due to their ability to enhance structural performance across various industries. These materials are widely employed in fields such as aerospace, chemical processing, electronics, and nuclear engineering [1, 2]. Rotating disks play a crucial role in many mechanical systems, such as ship propellers, compressors, pumps, and turbines. They have been widely studied under various loading conditions and geometric configurations to enhance durability, stability, and efficiency in engineering systems [3-6]. Additionally, these materials are primarily used in various industries and under natural environmental conditions, such as humidity and temperature changes [7]. Multilayered materials are increasingly used due to their superior performance in controlling displacement and distributing stress compared to single-layered ones. Under various loading conditions and over time, the occurrence of creep leads to noticeable changes in the material's microstructure, stress distribution, and displacements. Therefore, evaluating creep behavior under hygrothermal conditions is essential to ensure the structural performance and reliability of these materials.

The multiphysical behavior of different structures has been explored in numerous published studies. Karimi Zeverdejani and Kiani [8] established the influence of thermal shocks on the complex thermoelastic modeling of a hollow functionally graded sphere. Ganczarski and Szubartowski [9] examined the thermoelastic stresses of FGM plates employing the Sneddon–Lockett theorem. Karimi Zeverdejani and Kiani [8] established the effects of thermal shocks on the complex thermoelastic modeling of a hollow functionally graded sphere. Using a numerical approach, the stress response of an FGM shell bonded with sensors and actuators under magnetic, thermal, and electric loads was studied by Saadatfar and Aghaie-Khafri [10]. Likewise, they [7] showed that the efficiency of a functionally graded piezoelectric sensor and actuator varies significantly with the grading index under simultaneous magnetic, thermal, and electric loads. Saadatfar and Aghaie-Khafri subsequently carried out a comprehensive set of studies on short-length FGM cylindrical shells with functionally graded piezoelectric material (FGPM) layers. Their investigations involved various coupled field responses, including magneto-thermo-electro-mechanical [11], hygro-thermo-electro-mechanical [12], and hygro-thermo-magneto-electro-mechanical [13] behaviors. Yaghoobi et al. [14] presented a mathematical model for thermal buckling of piezoelectric FGM plates with temperature-dependent characteristics by utilizing a new power series Frobenius approach for calculating the decoupled governing equations for six boundary conditions. Arefi et al. [15] developed a new neutral surface-based sinusoidal shear deformation theory for examining FGPM plates, demonstrating its better accuracy in predicting bending behavior. Zenkour [16] conducted an analytical study providing a closed-form expression to describe the stress field of a thick-walled cylindrical structure, reinforced with piezoelectric fibers and FGM across the wall thickness when exposed to combined thermal and moisture effects. Harsha and Kumar [17] conducted a study on the dynamic stability and buckling performance of bidirectional porous FGPM plates placed on elastic foundations, analyzingthe interaction of porosity distributions, thermoelectric loads, and boundary conditions.

Numerous investigations focused on the creep analysis of smart and FGM structures. Singh et al. [18] applied finite element modeling to investigate the creep evolution in an FGM disc, revealing that raising the SiCp gradient enhances stress distribution, reduces strain rates, and extends rupture time. Sahni et al. [19] discovered that at high-pressure or rotation, exponential profiles most effectively reduce creep effects. Abdolkhani and Hashemian [20] examined creep in an autofrettage FGM vessel, showing that plastic depth and material grading significantly affect stress and strain trends. Using Sherby's law, Gupta et al. [21, 22] studied the creep evolution in an FGM annular plate with a radial thermal gradient. Later, Dharmpal et al. [23] presented a mathematical model to analyze steady-state creep in an FGM rotating disc with variable thickness. A creep study of an FGM disc with non-constant thickness was provided by Deepak [24]. Under thermal gradation, Rattan et al. [25] examined the creep performance of an FGM disc. Shariyat and Ghafourinam [26] studied creep in FGM spheres under hygrothermal effects, showing that moisture and temperature dependencies shift stress and strain distributions over time. Hosseini Kordkheili and Livani [27] conducted a creep study of an FGM annular plate with varying thickness in a thermal environment. Dharmpal et al. [28] presented a creep analysis for an FGM disc with non-constant thickness. Steady-state creep in Al–SiC FGM beams shows decreasing stress and curvature over time, especially with higher grading index, as reported by Golmakaniyoon and Akhlaghi [29]. Gupta and Singh

[30] developed a theoretical model for the creep behavior of rotating disks, considering both homogeneous and FGMs with non-uniform thickness profile configurations. Bose and Rattan [31] performed a comprehensive analysis of the creep process in a rotating FGM disk exhibiting parabolic property variation, subjected to thermal loading conditions. Loghman et al. [32] examined the thermoelastic creep behavior of an FGPM annular plate. Saadatfar et al [33] investigated the impacts of a heat source and convection boundaries on the creep behavior of a rotating smart FGM disc with variable thickness. Also, they [34] studied thermoelastic creep behavior in an FGPM rotating disc, including conduction, convection, and radiation, using the differential transformation method. The study of creep relaxation in FGM rotating discs with nonlinear material gradation was conducted by Zharfi [35], revealing significant variations in stress and strain rates subjected to steady-state conditions. Daghigh et al. [36] investigated time-dependent creep in ultra-high-temperature FGM rotating disks with variable thickness, showing that stress and displacement change significantly over time across different disk geometries. Zharfi et al. [36] performed creep analysis of thick FGM rotating disks with 2D gradation, showing that 2D modeling better captures stress and deformation behavior over time. Abdalla et al. [37] employed the finite element method along with numerical optimization to analyze and enhance the stress response of rotating functionally graded annular plates.

Regarding multi-layered structures, Farukoğlu and Korkut [38] examined failure stresses in multilayered fiber-reinforced rotating disks, showing that increasing reinforcement towards the outer radius improves strength under high-speed rotation. Akbarzadeh and Pasini [39] examined the impact of imperfect bonding and hygrothermal loads on multi-layered cylinders. To evaluate thermoelastic instability in multi-layered friction discs, Suo et al. [40] created a 2D FEM model. Ghatage et al. [41] thoroughly examined numerical modeling techniques for multi-directional FG beams, plates, and shells, evaluating their benefits over typical unidirectional FGMs. Several researchers have investigated imperfect interfacial bonding in multilayer structures. Wang [42] studied dynamic electromechanical responses in triple-layer piezoelectric cylinders with weak interfaces. Li and Lee [43] analyzed the fracture behavior of FGPM sensors with mechanically and electrically imperfect interfaces. Guinovart-Sanjuán et al. [44] investigated the effective elastic properties of laminated shell composites under weak interlayer contact using homogenization techniques. Wang et al. [45] explored vibration of layered quasicrystal plates with interfacial slips. Shaat et al. [46] presented an analytical model for thermomechanical loading in multilayered systems with imperfect bonding.

The literature review shows that no reported work exists on the creep response of multi-layered FGM discs with imperfect bonding subjected to hygrothermal environments. Therefore, for the first time, this study uses Norton's creep law and Prandtl–Reuss constitutive relations to explore the hygro-thermo-elastic creep evolution in a rotating multi-layered variable thickness FGM disc considering weak interlayer bonding.

## 2. Equations

### *2.1. Basic Equations*

Consider a rotating multi-layered non-uniform thickness functionally graded disk whose geometric configuration illustrated in Fig. 1. The bonding between the layers is assumed to be imperfect. The disc is placed within a hygrothermal environment, subjected to temperature, moisture, and an axial magnetic field. Axisymmetric conditions and the plane stress state were utilized in the analysis. Under axisymmetric conditions, all variables are independent of the circumferential direction ($\theta$).

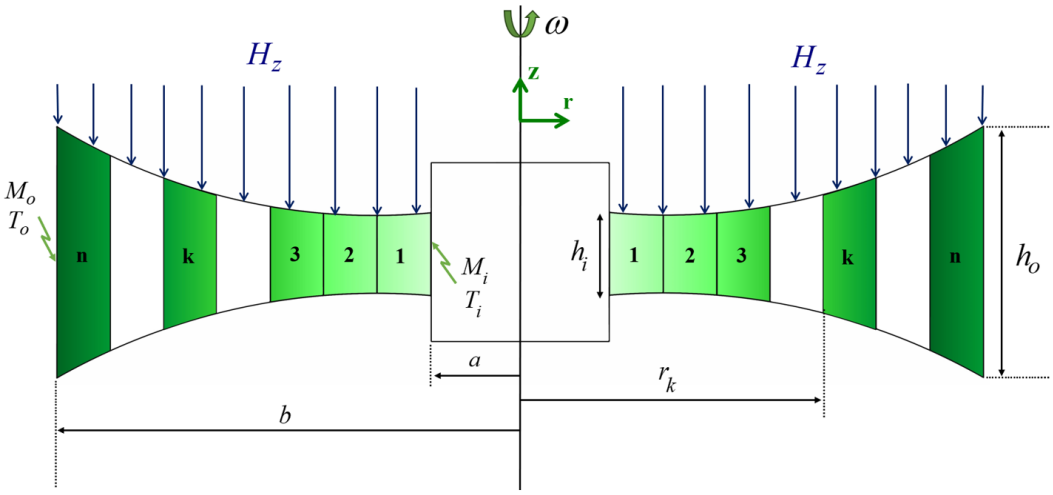


**Fig. 1.** A Multi-layered functionally graded disc.

Also, due to the plane stress assumption, the stress component in the axial direction is considered zero. Hence, the nonzero components of temperature, moisture concentration, and displacement are function of radius. The disk's thickness changes as a power-law distribution that varies radially:

$$h(r) = y_0 r^{\Omega} \tag{1}$$

where $y_0$ is a reference thickness and $\Omega$ is the thickness variation index. Since the material is functionally graded, all of its properties, such as elastic coefficients, density, and other relevant parameters, are assumed to vary as functions of the radius as a power-law expression, except for Poisson's ratio, which is assumed constant. In the following function, the overbar symbols ($\bar{\mathrm{K}}$) represent the material constants, and $\gamma$ denotes the inhomogeneity index:

$$\mathrm{K}(r) = \bar{\mathrm{K}}\, r^{\gamma} \tag{2}$$

### *2.2. Hygrothermal Equations*

The temperature and moisture concentration distributions can be determined independently [47]. Considering the FGM properties, axisymmetric conditions, and the absence of internal sources, the steady-state equation is governed by Fourier's law of heat conduction and Fick's law for moisture diffusion, as presented below [48, 49]:

$$\frac{1}{r}\frac{\partial}{\partial r}\left(rh(r)k^T(r)\frac{\partial T}{\partial r}\right) = 0 \tag{3}$$

$$\frac{1}{r}\frac{\partial}{\partial r}\left(rh(r)k^M(r)\frac{\partial M}{\partial r}\right) = 0 \tag{4}$$

where, T denotes the temperature field and M represents the moisture concentration. These equations can be rewritten using Eqs. (1) and (2) as:

$$\frac{1}{r}\frac{\partial}{\partial r}\left(r^{\gamma+\Omega+1}k^T\frac{\partial T}{\partial r}\right) = 0 \tag{5}$$

$$\frac{1}{r}\frac{\partial}{\partial r}\left(r^{\gamma+\Omega+1}k^M\frac{\partial M}{\partial r}\right) = 0 \tag{6}$$

Integrating Eqs. (5) and (6) twice yields:

$$T(r) = a_1 r^{-\gamma-\Omega} + a_2 \tag{7}$$

$$M(r) = b_1 r^{-\gamma-\Omega} + b_2 \tag{8}$$

The hygrothermal boundary conditions and the imperfect bonding conditions at the interfaces between the $i_{th}$ and $(i+1)_{th}$ layers are defined as follows:

$$\begin{aligned} &T_1(r)|_{r=a} = T_a, \\ &T_n(r)|_{r=b} = T_b \end{aligned}$$

$$\begin{aligned} &k_i^T(r)\left.\frac{\partial T_i}{\partial r}\right|_{r=r_i} = k_{i+1}^T(r)\left.\frac{\partial T_{i+1}}{\partial r}\right|_{r=r_i} \\ &T_i|_{r=r_i} - T_{i+1}|_{r=r_i} = \chi_i^T k_i^T(r)\left.\frac{\partial T_i}{\partial r}\right|_{r=r_i} \end{aligned} \tag{9}$$

$$\begin{aligned} &M_1(r)|_{r=a} = M_a, \\ &M_n(r)|_{r=b} = M_b \\ &k_i^M(r)\left.\frac{\partial M_i}{\partial r}\right|_{r=r_i} = k_{i+1}^M(r)\left.\frac{\partial M_{i+1}}{\partial r}\right|_{r=r_i} \\ &M_i|_{r=r_i} - M_{i+1}|_{r=r_i} = \chi_i^M k_i^M(r)\left.\frac{\partial M_i}{\partial r}\right|_{r=r_i} \end{aligned} \tag{10}$$

The linear spring model was considered due to the thermal field discontinuity, in which the parameters $\chi_i^T$ and $\chi_i^M$ represent the thermal and moisture compliance associated with the imperfect bonding at the interfaces, respectively [13, 50]. Under perfect bonding conditions, both parameters are assumed to be zero. By solving two algebraic systems obtained from Eq. (9), the $2n$ unknown constants for the functionally graded disk with $n$ layers were determined.

### *2.3. Stress Equations*

The total strain was considered as the combined effect of creep, elastic, and hygrothermal components. Accordingly, the stress–strain relationships were formulated as follows [51, 52]:

$$\begin{aligned} \sigma_r = {} & c_{11}(\varepsilon_{rr} - \varepsilon_{rr}^c) + c_{12}(\varepsilon_{\theta\theta} - \varepsilon_{\theta\theta}^c) + c_{13}(\varepsilon_{zz} - \varepsilon_{zz}^c) \\ & - \lambda_1 T - \zeta_1 M \end{aligned} \tag{11}$$

$$\begin{aligned} \sigma_\theta = {} & c_{12}(\varepsilon_{rr} - \varepsilon_{rr}^c) + c_{22}(\varepsilon_{\theta\theta} - \varepsilon_{\theta\theta}^c) + c_{23}(\varepsilon_{zz} - \varepsilon_{zz}^c) \\ & - \lambda_2 T - \zeta_2 M \end{aligned} \tag{12}$$

$$\begin{aligned} \sigma_z = {} & c_{13}(\varepsilon_{rr} - \varepsilon_{rr}^c) + c_{23}(\varepsilon_{\theta\theta} - \varepsilon_{\theta\theta}^c) + c_{33}(\varepsilon_{zz} - \varepsilon_{zz}^c) \\ & - \lambda_3 T - \zeta_3 M \end{aligned} \tag{13}$$

where, $c_{ij}$, $\lambda_i$ and $\zeta_i$ represent the elastic constants and the thermal and moisture moduli, respectively. Also, the superscript $c$ indicates the creep strain components. The strain-displacement and hygrothermal modulus relations are given as:

$$\varepsilon_{rr} = \frac{\partial u}{\partial r}, \qquad \varepsilon_{\theta\theta} = \frac{u}{r}. \tag{14}$$

$$\left\{\begin{array}{l} \lambda_1 = c_{11}\alpha_r + c_{12}\alpha_\theta + c_{13}\alpha_z \\ \lambda_2 = c_{12}\alpha_r + c_{22}\alpha_\theta + c_{23}\alpha_z \\ \lambda_3 = c_{13}\alpha_r + c_{23}\alpha_\theta + c_{33}\alpha_z \end{array}\right\},$$

$$\left\{\begin{array}{l} \zeta_1 = c_{11}\beta_r + c_{12}\beta_\theta + c_{13}\beta_z \\ \zeta_2 = c_{12}\beta_r + c_{22}\beta_\theta + c_{23}\beta_z \\ \zeta_3 = c_{13}\beta_r + c_{23}\beta_\theta + c_{33}\beta_z \end{array}\right\} \tag{15}$$

where, $\alpha_i$ and $\beta_i$ denote the thermal and moisture expansion coefficients, respectively. Concerning the plane

stress state ($\sigma_z = 0$) and the disk's functionally graded nature, Eqs. (11)-(10) can be rewritten as follows:

$$\sigma_r = C_1 r^{\gamma}\frac{\partial u}{\partial r} + C_2 r^{\gamma}\frac{u}{r} - \lambda_1' r^{2\gamma}T - \zeta_1' r^{2\gamma}M - C_1 r^{\gamma}\varepsilon_{rr}^{c} - C_2 r^{\gamma}\varepsilon_{\theta\theta}^{c} \quad (16)$$

$$\sigma_\theta = E_1 r^{\gamma}\frac{\partial u}{\partial r} + E_2 r^{\gamma}\frac{u}{r} - \lambda_2' r^{2\gamma}T - \zeta_2' r^{2\gamma}M - E_1 r^{\gamma}\varepsilon_{rr}^{c} - E_2 r^{\gamma}\varepsilon_{\theta\theta}^{c} \quad (17)$$

Where,

$$C_1 = c_{11} - \frac{c_{13}^2}{c_{33}}, \quad C_2 = E_1 = c_{12} - \frac{c_{13}c_{23}}{c_{33}},$$
$$E_2 = c_{22} - \frac{c_{23}^2}{c_{33}}, \quad \lambda_1' = \lambda_1 - \frac{c_{13}\lambda_3}{c_{33}}, \quad (18)$$
$$\lambda_2' = \lambda_2 - \frac{c_{23}\lambda_3}{c_{33}}, \quad \zeta_1' = \zeta_1 - \frac{c_{13}\zeta_3}{c_{33}},$$
$$\zeta_2' = \zeta_2 - \frac{c_{23}\zeta_3}{c_{33}}.$$

The Lorentz force is formulated based on the following equations [53]:

$$\begin{aligned}
&\vec{h} = \nabla \times (\vec{u} \times \vec{H}),\\
&\vec{E} = -(\overrightarrow{\vec{u}} \times \vec{H})\mu,\\
&\vec{J} = -\varepsilon_e \frac{d\vec{E}}{dt} + \nabla \times \vec{h},\\
&\vec{f} = (\vec{J} \times \vec{H})\mu.
\end{aligned} \quad (19)$$

The Lorentz force induced by the applied axial magnetic field is expressed as follows:

$$f_r = \mu H_z^2\left(\frac{\partial^2 u}{\partial r^2} + \frac{1}{r}\frac{\partial u}{\partial r} - \frac{u}{r^2}\right) \quad (20)$$

The nonzero terms of the equilibrium equation for the disc are as follows:

$$\frac{\partial\left(h(r)\sigma_r\right)}{\partial r} + h(r)\frac{(\sigma_r - \sigma_\theta)}{r} + h(r)\rho r\omega^2 + h(r)f_r = 0 \quad (21)$$

Substituting Eqs. (20), (16), and (17) into Eq. (21) yields the following result:

$$\begin{aligned}
&\frac{\partial^2 u}{\partial r^2} + \frac{M_1}{r}\frac{\partial u}{\partial r} + \frac{M_2}{r^2}u = M_3 r^{\gamma-1}T + \left(M_6 r^{\gamma}\right)\frac{\partial T}{\partial r}\\
&+ M_9 r^{\gamma-1}M\\
&+ \left(M_{12}r^{\gamma}\right)\frac{\partial M}{\partial r} - M_{13}r + M_{14}r^{-1}\varepsilon_{rr}^{c} + M_{17}\frac{\partial \varepsilon_{rr}^{c}}{\partial r}\\
&+ M_{15}r^{-1}\varepsilon_{\theta\theta}^{c} + M_{16}\frac{\partial \varepsilon_{\theta\theta}^{c}}{\partial r}
\end{aligned} \quad (22)$$

Where,

$$\begin{aligned}
M_1 &= \frac{\bar{\mu}H_z^2 + (\gamma + \Omega + 1)C_1}{\bar{\mu}H_z^2 + C_1},\\
M_2 &= \frac{(\gamma + \Omega)C_2 - E_2 - \bar{\mu}H_z^2}{\bar{\mu}H_z^2 + C_1}\\
M_3 &= \frac{(2\gamma + \Omega + 1)\lambda_1' - \lambda_2'}{\bar{\mu}H_z^2 + C_1}, \quad M_6 = \frac{\lambda_1'}{\bar{\mu}H_z^2 + C_1}\\
M_9 &= \frac{(2\gamma + \Omega + 1)\zeta_1' - \zeta_2'}{\bar{\mu}H_z^2 + C_1}, \quad M_{12} = \frac{\zeta_1'}{\bar{\mu}H_z^2 + C_1},\\
M_{13} &= \frac{\rho\omega^2}{\bar{\mu}H_z^2 + C_1}, \quad M_{14} = \frac{(\gamma + \Omega + 1)C_1 - E_1}{\bar{\mu}H_z^2 + C_1},\\
M_{15} &= \frac{(\gamma + \Omega + 1)C_2 - E_2}{\bar{\mu}H_z^2 + C_1},\\
M_{16} &= \frac{C_2}{\bar{\mu}H_z^2 + C_1}, \quad M_{17} = \frac{C_1}{\bar{\mu}H_z^2 + C_1}.
\end{aligned} \quad (23)$$

## 3. Solution

### 3.1. Initial Solution

Neglecting the creep strain terms in Eq. (22), one can write:

$$\begin{aligned}
&\frac{\partial^2 u}{\partial r^2} + \frac{M_1}{r}\frac{\partial u}{\partial r} + \frac{M_2}{r^2}u = M_3 r^{\gamma-1}T + M_6 r^{\gamma}\frac{\partial T}{\partial r}\\
&- M_{13}r + M_9 r^{\gamma-1}M + M_{12}r^{\gamma}\frac{\partial M}{\partial r}
\end{aligned} \quad (24)$$

Replacing Eqs. (7), and (8) into Eq. (24) gives:

$$\begin{aligned}
&\frac{\partial^2 u}{\partial r^2} + \frac{M_1}{r}\frac{\partial u}{\partial r} + \frac{M_2}{r^2}u = \left(M_3 a_1 + M_6 a_1(-\gamma - \Omega)\right.\\
&+ M_9 b_1 + M_{12} b_1(-\gamma - \Omega)r^{-\Omega-1}\\
&\left.+ \left(M_3 a_2 + M_9 b_2\right)r^{\gamma-1} - M_{13}r\right.
\end{aligned} \quad (25)$$

The solution to the above equation is expressed as the homogeneous (general) solution plus a particular solution:

$$\begin{aligned}
u = u_g + u_p = &\underbrace{\left(B_1 r^{m_1} + B_2 r^{m_2}\right)}_{u_g}\\
&+ \underbrace{\left(B_3 r^{-\Omega+1} + B_4 r^{\gamma+1} + B_7 r^3\right)}_{u_p}
\end{aligned} \quad (26)$$

where, $B_1$ and $B_2$ are unknown values, and we have:

$$\begin{aligned}
m_{1,2} &= \frac{1}{2}\left(-(M_1 - 1) \pm \sqrt{(M_1 - 1)^2 - 4M_2}\right),\\
B_3 &= \frac{M_3 a_1 + M_6 a_1(-\gamma - \Omega) + M_9 b_1 + M_{12} b_1(-\gamma - \Omega)}{(-\Omega + 1)^2 - (-\Omega + 1) + M_1(-\Omega + 1) + M_2}\\
B_4 &= \frac{(M_3 a_2 + M_9 b_2)}{(\gamma + 1)^2 - (\gamma + 1) + M_1(\gamma + 1) + M_2},\\
B_7 &= \frac{-M_{13}}{6 + 3M_1 + M_2},
\end{aligned} \quad (27)$$

Now, Eqs. (16) and (17) can be reformulated using Eqs. (7), (8), and (26):

$$\begin{aligned}\sigma_r &= (C_1 m_1 + C_2)\, B_1 r^{\gamma+m_1-1} \\ &+ ((C_1(-\Omega+1)+C_2)\, B_3 - \lambda_1' a_1 - \zeta_1' b_1)\, r^{\gamma-\Omega} \\ &+ ((C_1(\gamma+1)+C_2)\, B_4 - \lambda_1' a_2 - \zeta_1' b_2)\, r^{2\gamma} \\ &+ (3C_1+C_2)\, B_7 r^{\gamma+2} + (C_1 m_2 + C_2)\, B_2 r^{\gamma+m_2-1} \end{aligned} \quad (28)$$

$$\begin{aligned}\sigma_\theta &= (E_1 m_1 + E_2)\, B_1 r^{\gamma+m_1-1} \\ &+ ((E_1(-\Omega+1)+E_2)\, B_3 - \lambda_2' a_1 - \zeta_2' b_1)\, r^{\gamma-\Omega} \\ &+ ((E_1(\gamma+1)+E_2)\, B_4 - \lambda_2' a_2 - \zeta_2' b_2)\, r^{2\gamma} v \\ &+ (3E_1+E_2)\, B_7 r^{\gamma+2} + (E_1 m_2 + E_2)\, B_2 r^{\gamma+m_2-1} \end{aligned} \quad (29)$$

The disc can be subjected to different mechanical boundary conditions. For example, the clamp-free condition can be defined as follows:

$$\begin{aligned} u_r^{(1)}(a) &= 0, \\ \sigma_r^{(n)}(b) &= 0\ . \end{aligned} \quad (30)$$

Imperfect interlayer bonding leads to the following interface conditions between $i_{th}$ and $(i+1)_{th}$layers [13]:

$$\begin{aligned} &\sigma_r^{(i)}(r_i) = \sigma_r^{(i+1)}(r_i), \\ &u_r^{(i+1)}(r_i) - u_r^{(i)}(r_i) = \chi_i^u \sigma_r^{(i)}(r_i). \end{aligned} \quad (31)$$

The unknown constants for each layer, denoted as $B_1{}^{(i)}$, and $B_2{}^{(i)}$, can be calculated by solving the resulting system of *2n* algebraic equations for the unknowns. The solution of this system yields initial field values at t=0.

### *3.2. Creep Solution*

Under steady hygrothermal conditions, differentiating Eq. (22) with respect to time gives:

$$\begin{aligned}&\frac{\partial^2 \dot{u}}{\partial r^2} + \frac{M_1}{r}\frac{\partial \dot{u}}{\partial r} + \frac{M_2}{r^2}\dot{u} = M_{14} r^{-1}\dot{\varepsilon}_{rr}^c + M_{17}\frac{\partial \dot{\varepsilon}_{rr}^c}{\partial r} \\ &+ M_{15} r^{-1}\dot{\varepsilon}_{\theta\theta}^c + M_{16}\frac{\partial \dot{\varepsilon}_{\theta\theta}^c}{\partial r} \end{aligned} \quad (32)$$

The creep strain rates are expressed by the Prandtl-Reuss relations as:

$$\begin{aligned} \dot{\varepsilon}_{rr}^c &= \frac{\dot{\varepsilon}_e^c}{\sigma_e}\left(\sigma_r - \frac{\sigma_\theta+\sigma_z}{2}\right) \\ \dot{\varepsilon}_{\theta\theta}^c &= \frac{\dot{\varepsilon}_e^c}{\sigma_e}\left(\sigma_\theta - \frac{\sigma_r+\sigma_z}{2}\right) \\ \dot{\varepsilon}_{zz}^c &= \frac{\dot{\varepsilon}_e^c}{\sigma_e}\left(\sigma_z - \frac{\sigma_r+\sigma_\theta}{2}\right) \end{aligned} \quad (33)$$

Here, $\dot{\varepsilon}_i^c$ denotes the creep strain rate, $\dot{\varepsilon}_e^c$ represents the effective creep strain rate, and $\sigma_e$ corresponds to the effective stress. The creep behavior is described using Norton's law, expressed as follows:

$$\dot{\varepsilon}_e^c = B(r)\, \sigma_e^{n\,(r)} = (b_0\, r^{b_1})\, \sigma_e^{n_0} \quad (34)$$

The parameters $n_0$, $b_1$, and $b_0$ are constants. Considering the plane-stress state, Eqs. (33) results in:

$$\begin{aligned} \dot{\varepsilon}_{rr}^c &= b_0 r^{b_1} \sigma_e^{n_0-1}(\sigma_r - 0.5\sigma_\theta) \\ \dot{\varepsilon}_{\theta\theta}^c &= b_0 r^{b_1} \sigma_e^{n_0-1}(\sigma_\theta - 0.5\sigma_r) \\ \dot{\varepsilon}_{zz}^c &= -b_0 r^{b_1} \sigma_e^{n_0-1}(\dot{\varepsilon}_{rr}^c + \dot{\varepsilon}_{\theta\theta}^c) \end{aligned} \quad (35)$$

The equivalent stress, according to the Von-Mises criterion, is given by:

$$\sigma_{eq} = \sqrt{\sigma_r^2 + \sigma_\theta^2 - \sigma_r\sigma_\theta} \quad (36)$$

The solution to Eq. (32) was given by:

$$\dot{u} = D_1 r^{m_1} + D_2 r^{m_2} + G_1(r) r^{m_1} + G_2(r) r^{m_2} \quad (37)$$

The functions $G_1(r)$ and $G_2(r)$ can be determined using the variation of parameters method, as follows:

$$\begin{aligned} G_1(r) &= \frac{1}{m_2-m_1}\int \Bigg\{ r^{1-m_1} \\ &\left( M_{14} r^{-1}\dot{\varepsilon}_{rr}^c + M_{17}\frac{\partial \dot{\varepsilon}_{rr}^c}{\partial r} + M_{15} r^{-1}\dot{\varepsilon}_{\theta\theta}^c \right. \\ &\left. + M_{16}\frac{\partial \dot{\varepsilon}_{\theta\theta}^c}{\partial r} \right) dr \end{aligned} \quad (38)$$

$$\begin{aligned} G_2(r) &= -\frac{1}{m_2-m_1}\int \Bigg\{ r^{1-m_2} \\ &\left( M_{14} r^{-1}\dot{\varepsilon}_{rr}^c + M_{17}\frac{\partial \dot{\varepsilon}_{rr}^c}{\partial r} + M_{15} r^{-1}\dot{\varepsilon}_{\theta\theta}^c \right. \\ &\left. + M_{16}\frac{\partial \dot{\varepsilon}_{\theta\theta}^c}{\partial r} \right) dr \end{aligned}$$

The derivative of Eqs. (16) and (17) with time gives:

$$\dot{\sigma}_r = C_1 r^\gamma \frac{\partial \dot{u}}{\partial r} + C_2 r^\gamma \frac{\dot{u}}{r} - C_1 r^\gamma \dot{\varepsilon}_{rr}^c - C_2 r^\gamma \dot{\varepsilon}_{\theta\theta}^c \quad (39)$$

$$\dot{\sigma}_\theta = E_1 r^\gamma \frac{\partial \dot{u}}{\partial r} + E_2 r^\gamma \frac{\dot{u}}{r} - E_1 r^\gamma \dot{\varepsilon}_{rr}^c - E_2 r^\gamma \dot{\varepsilon}_{\theta\theta}^c \quad (40)$$

At last, substituting Eq. (35) and (37) into (39) and (40) yields:

$$\begin{aligned} \dot{\sigma}_r &= (C_1 m_1 (D_1+G_1) + C_2 (D_1+G_1))\, r^{\gamma+m_1-1} \\ &+ (C_1 m_2 (D_2+G_2) + C_2 (D_2+G_2))\, r^{\gamma+m_2-1} \\ &+ \left(C_1 \frac{\partial G_1}{\partial r}\right) r^{\gamma+m_1} + \left(C_1 \frac{\partial G_2}{\partial r}\right) r^{\gamma+m_2} \\ &- (C_1(\sigma_r - 0.5\sigma_\theta) + C_2(\sigma_\theta - 0.5\sigma_r)) \\ &\quad r^{\gamma+b_1} b_0 \sigma_e^{n_0-1} \end{aligned} \quad (41)$$

$$\begin{aligned} \dot{\sigma}_\theta &= (E_1 m_1 (D_1+G_1) + E_2 (D_1+G_1))\, r^{\gamma+m_1-1} \\ &+ (E_1 m_2 (D_2+G_2) + E_2 (D_2+G_2))\, r^{\gamma+m_2-1} \\ &+ \left(E_1 \frac{\partial G_1}{\partial r}\right) r^{\gamma+m_1} + \left(E_1 \frac{\partial G_2}{\partial r}\right) r^{\gamma+m_2} \\ &- (E_1(\sigma_r - 0.5\sigma_\theta) + E_2(\sigma_\theta - 0.5\sigma_r)) \\ &\quad r^{\gamma+b_1} b_0 \sigma_e^{n_0-1} \end{aligned} \quad (42)$$

The unknown coefficients are determined through both the interlayer and boundary conditions. Since the boundary conditions at the inner and outer surfaces of the FGM disc remain unchanged, one can write:

$$\dot{u}_r^{(1)}(a) = 0, \qquad \dot{\sigma}_r^{(n)}(b) = 0. \tag{43}$$

Furthermore, the time derivative of Eq. (31) leads to the following interlayer conditions:

$$\begin{aligned} &\dot{\sigma}_r^{(i)}(r_i) = \dot{\sigma}_r^{(i+1)}(r_i), \\ &\dot{u}_r^{(i+1)}(r_i) - \dot{u}_r^{(i)}(r_i) = \chi_i^u \dot{\sigma}_r^{(i)}(r_i). \end{aligned} \tag{44}$$

Similar to the previous section, the resulting system of $2n$ algebraic equations can be formulated to find the unknown constants. Knowing the rates of various fields to get the history of them throughout the creep process is necessary. Initially, an appropriate time increment ($\mathrm{dt}^{(i)}$) must be selected to define the progression of time steps throughout the creep analysis. One way to display the total time after the $m_{th}$ step time is as follows:

$$t_i = \sum_{k=0}^{m} dt^{(k)} \tag{45}$$

At each time step, the rates of various fields are calculated using the known values from the previous step. Finally, the iterative update at the $m_{th}$ time step can be described as follows:

$$\begin{aligned} &\Phi_{(m)}(r, t_m) = \Phi_{(m-1)}(r, t_{m-1}) + \dot{\Phi}_{(m-1)}(r, t_{m-1}) dt_{(m)}, \\ &\Phi = u_r, \sigma_r, \sigma_\theta \end{aligned} \tag{46}$$

It should be mentioned that iterative methods typically solve the creep evolution equations using incremental time steps and update material properties iteratively. The computational cost of these methods is much lower than that of other numerical methods, such as finite element methods. It requires small time steps for accuracy and stability. Therefore, for simple boundary conditions, idealized shapes and straightforward material laws (such as Norton's law) are a good choice. Convergence is typically ensured through proper incremental time integration. For example, the backward Euler method is recommended for creep because it is unconditionally stable. Also, using an adaptive time-stepping algorithm can help adjust the time step if convergence is slow.

## 4. Numerical Results

This section presents several numerical examples to examine the influence of various parameters on the stress distribution and deformation of the disc. The material properties used are listed in Table 1. The following non-dimensional variables were employed in the graphs:

$$R = \frac{r - r_i}{r_o - r_i}, \quad \sigma_{r,\theta}^* = \frac{\sigma_{r,\theta}}{c_{11}}, \quad u_r^* = \frac{u_r}{r_i}. \tag{47}$$

A multi-layered rotating functionally graded disc with inner and outer radii of 0.07m and 0.35m was considered for the analysis. The numerical examples are based on the following parameter values:

$$\begin{aligned} &T_i = 0, && T_o = 50(K), \\ &M_i = 0, && M_o = 3\%, \\ &\omega = 50\pi(\mathrm{rad/s}) && \\ &y_0 = 0.027(\mathrm{m}), && \Omega = -0.55, \\ &H_z = 5 \times 10^4\,(A/m), && dt = 1 \times 10^7(s). \end{aligned} \tag{48}$$

As highlighted in Fig. 2, to validate the calculations, the findings were compared with the reported work on the static behaviors of a single-layer FGM disc [2, 54] displays a good agreement between the results for the radial stresses.

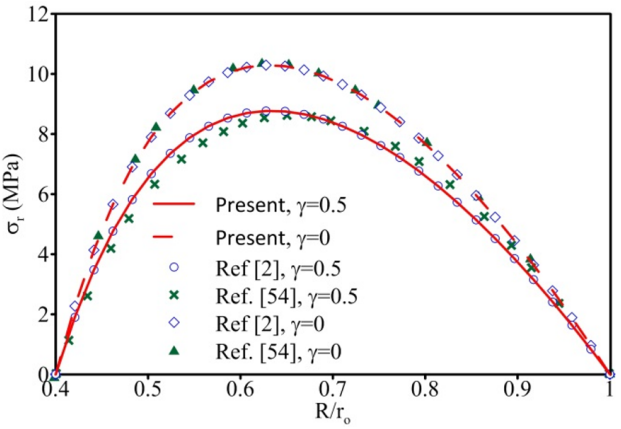


**Fig. 2.** Validation of results.

### *4.1. Creep (2D & 3D)*

Fig. 3 illustrates the time-dependent creep redistribution of various fields. In this case, a four-layered FGM disc is analyzed with properties and loadings defined according to Eq. (48). Over time, radial stress in each layer decreases, with a diminishing rate of decline. The peak radial stress gradually shifts from the inner radius toward intermediate radii and layers. The peak hoop stress at the outer layer diminishes gradually with time. Moreover, the jump in hoop stress at the interlayers reduces as creep progresses. Similarly, equivalent stress in all layers shows a consistent reduction, with interfacial jumps diminishing over time. In the static state, the maximum equivalent stress occurs at the outer radius of the inner layer, but due to creep, it shifts to the outer radius of the middle layer. Radial displacement increases with time, reaching its maximum at the outer boundary. For clearer insight, these distributions are also depicted in Fig. 4.

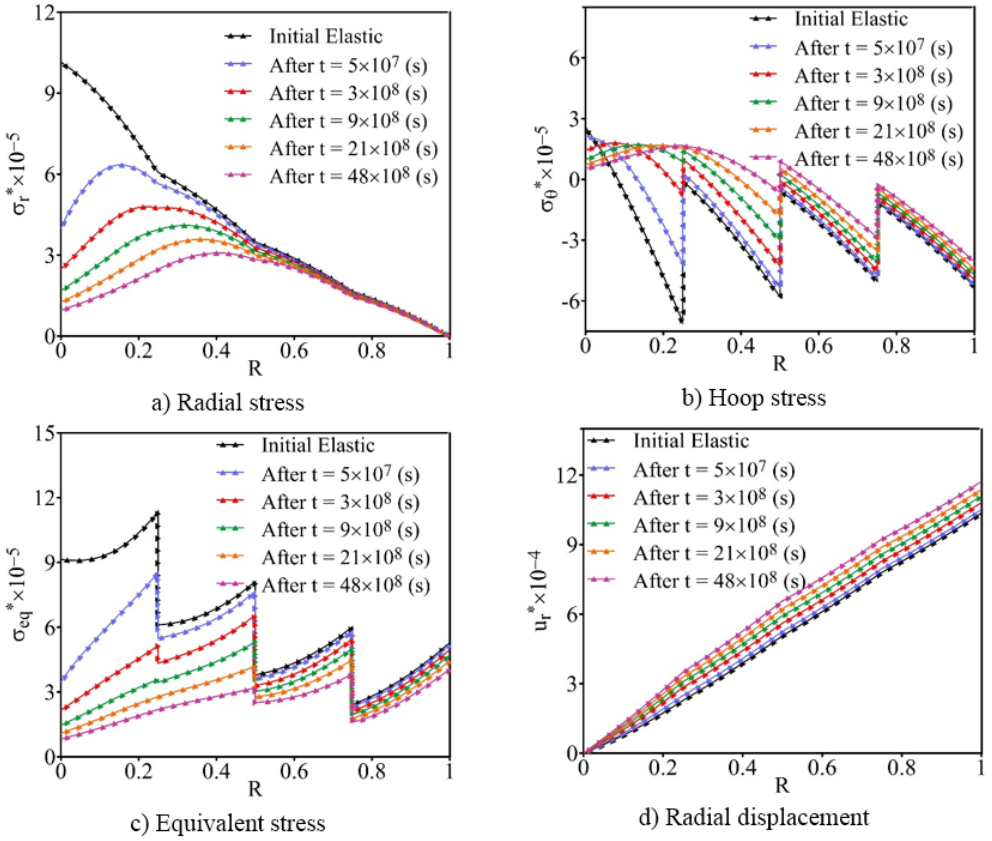


**Fig. 3.** Redistribution of parameters during creep evolution, $\gamma_1 = 0.25,\ \gamma_2 = 0.5,\ \gamma_3 = 0.75,\ \gamma_4 = 1$.

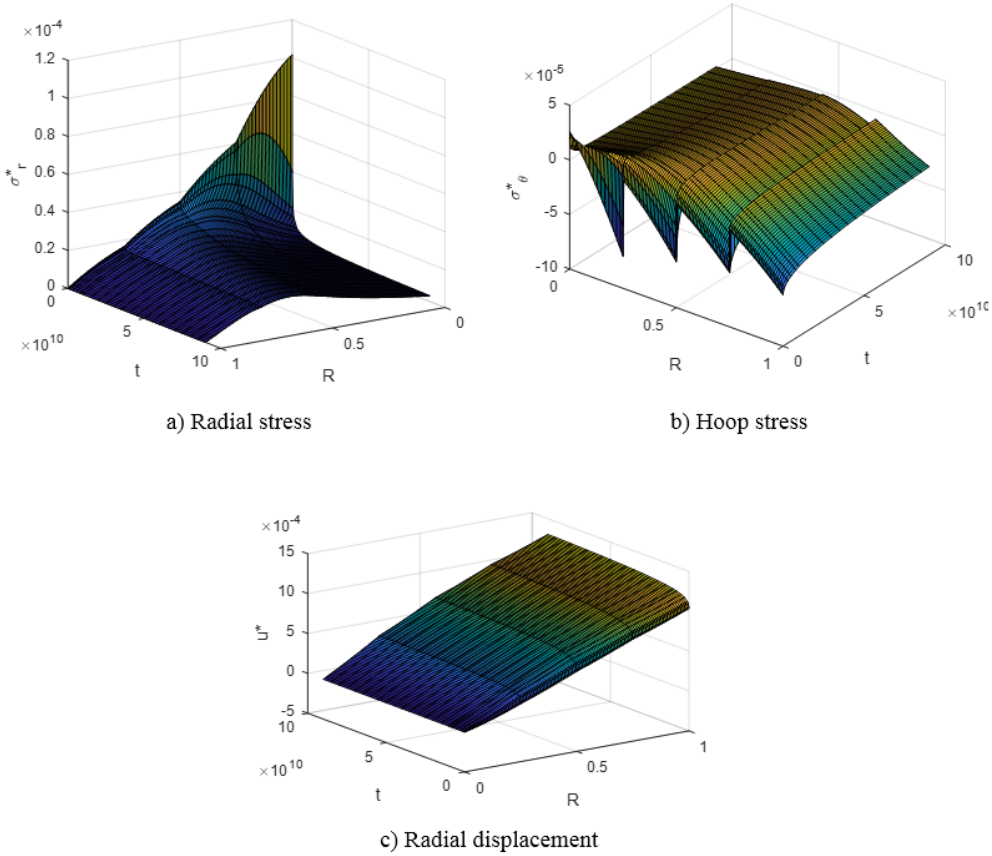


**Fig. 4.** Redistribution for various fields during creep evolution.

### *4.2. Angular Velocity*

The effect of angular velocity on both static and creep states is shown in Fig. 5. In this case, $dt = 1 \times 10^8$ and the other used parameters are as before. Radial stress increases with angular velocity, and the rate of this increase accelerates under both static and creep conditions, meaning it rises more with greater angular velocities. Given the brittle nature of FGM materials, particular care must be taken when the hoop stress becomes positive (tensile). In the static case, the maximum equivalent stress is located at the inner radius and grows progressively with angular velocity. Under creep conditions, the location of maximum equivalent stress initially lies at the outer radius for low angular velocities but shifts toward intermediate layers as the velocity increases. Additionally, in both cases, the interlayer stress jump diminishes with higher velocity. Overall, an increase in radial displacement is also observed with rising angular velocity.

### *4.3. Magnetic Field*

The impact of the axial magnetic field on the static and creep responses of a four-layer FGM rotating disc was investigated. As a simplifying assumption, it is considered that $H_Z^* = H_Z \times 10^8$.The parameters used are the same as previously. As shown in Fig. 6, radial stress increases with higher magnetic field. In the static state, the maximum increase occurs at the inner radius of the innermost layer, while during creep progression, this peak shifts toward the outer radius of the inner layer. Stronger magnetic fields lead to a maximum hoop stress at the outer radius of the inner layer and elevate hoop stress across all layers. Moreover, in both static and creep states, increasing the magnetic field intensifies the tensile hoop stress at the inner radius, potentially promoting crack initiation and growth. The equivalent stress increases with the rise in axial magnetic field magnitude. In the creep situation, the maximum equivalent stress occurs in the middle layers under lower magnetic fields, while higher magnetic fields shift it toward the inner layers. In addition, the plots indicate that radial displacement increases with higher axial magnetic field magnitude.

### *4.4. Hygrothermal Loading*

Fig. 7 illustrates the influence of hygrothermal loading on the static and creep responses of the disc, with all other parameters kept unchanged. Radial stress increases with rising hygrothermal loads, initially reaching its maximum at the inner radius of the inner layer initially, then shifting toward the outer radius of the same layer as the creep develops.

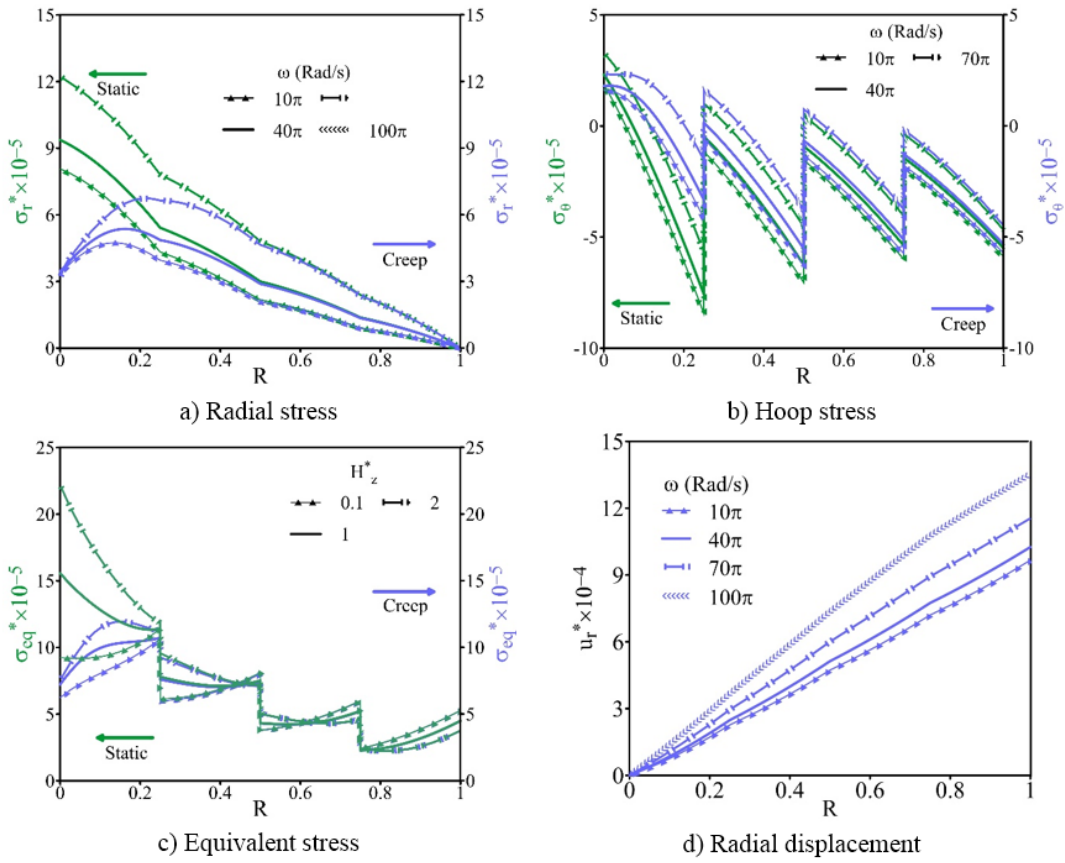


**Fig. 5.** Influence of angular velocity in both static and creep states. $\gamma_1 = 0.25$, $\gamma_2 = 0.5$, $\gamma_3 = 0.75$, $\gamma_4 = 1$. .

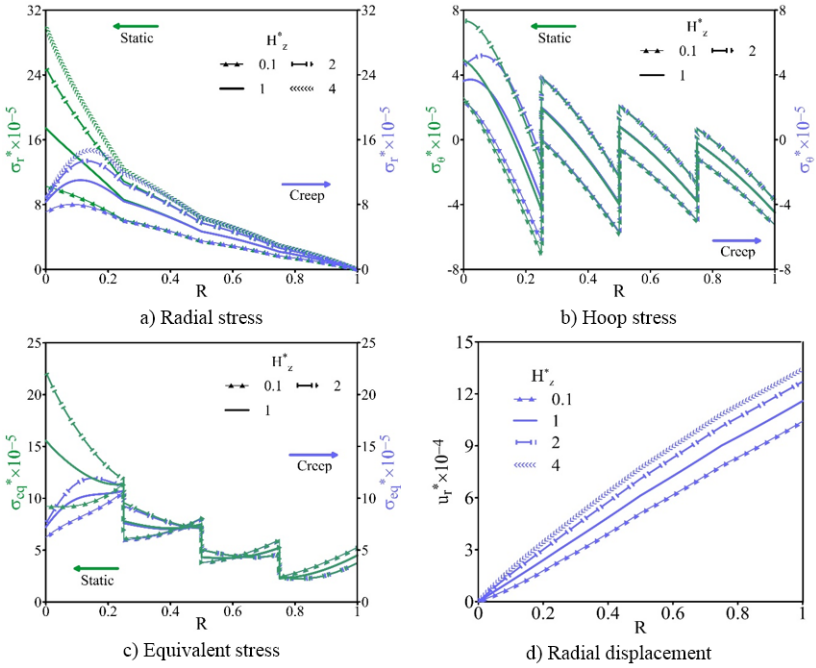


**Fig. 6.** Influence of the axial magnetic field in both static and creep states $\gamma_1 = 0.25,\ \gamma_2 = 0.5,\ \gamma_3 = 0.75,\ \gamma_4 = 1$.

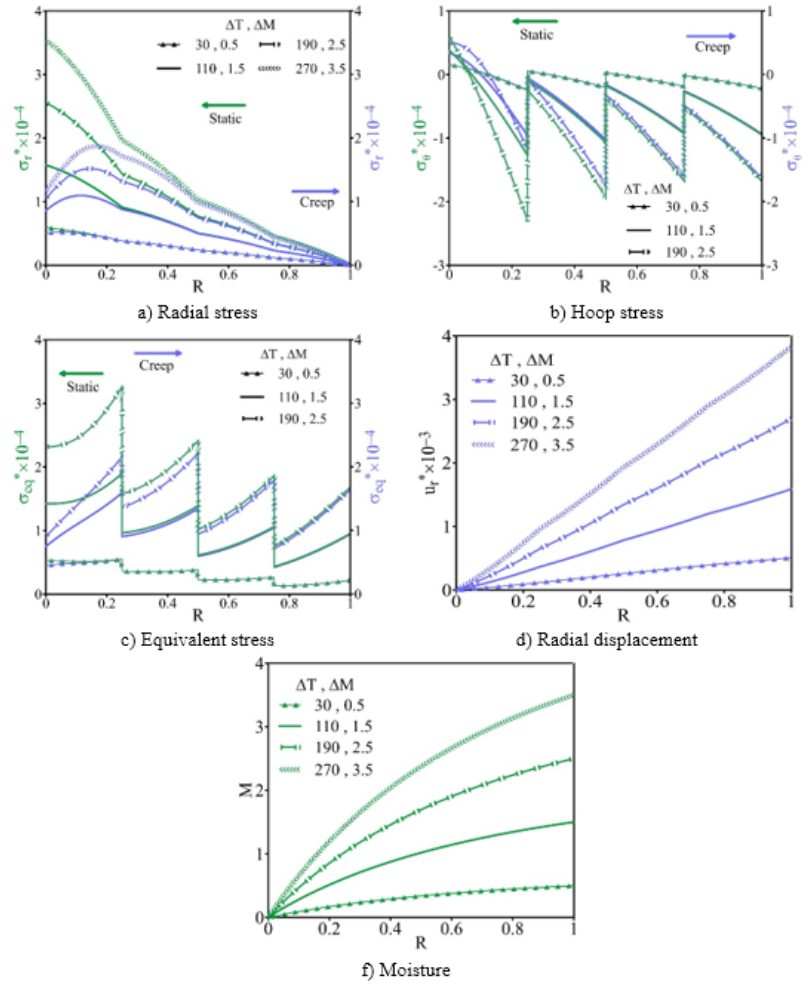


**Fig. 7.** Influence of the hygrothermal loading in both static and creep states $\gamma_1 = 0.25,\ \gamma_2 = 0.5,\ \gamma_3 = 0.75,\ \gamma_4 = 1$.

Increased hygrothermal loading also amplifies the tensile hoop stress at the inner radius, which is critical given the brittle nature of FGMs and the risk of crack initiation. Additionally, the maximum hoop stress at the outer radius rises with higher hygrothermal loads. Equivalent stress similarly increases, accompanied by a more pronounced interlayer stress jump. Radial displacement grows under both static and creep conditions, with its peak occurring at the outer radius due to the clamp-free boundary condition. The graphs also indicate that moisture concentration rises with increasing hygrothermal loads. For brevity, temperature plots have been excluded, as temperature and moisture follow similar trends and governing equations.

### *4.5. Imperfect Bounding*

Fig. 8 displays the effect of imperfect bonding on the behavior of the multilayer FGM disc. As before, the same parameters were used. To simplify the analysis, uniform bonding imperfections were assumed across all interlayers. The imperfection constants were defined as$\chi^u = 9\times10^{-13}A,\ \chi^T = 5\times10^{-3}A,\ \chi^M = 5\times10^{-3}A$. According to the graph, radial stress decreases with increasing imperfection coefficients in both static and creep situations, with the static case exhibiting a more significant reduction. Additionally, the creep hoop stress is largest in the outer layer and reduces as the imperfection coefficient increases. Similarly, the equivalent stress decreases with greater imperfection coefficient. The radial displacement graph indicates that weak bonding leads to increased displacement in the outer layer and reduced displacement in the inner layer. As expected, imperfect bonding introduces noticeable jumps in the displacement profile at the interlayer interfaces, which become more pronounced with higher imperfection coefficients. A similar discontinuity is observed in the temperature distribution, where temperature rises in the outer layer and drops in the inner layer due to interfacial imperfections. Moisture concentration follows a similar trend to temperature but is omitted for brevity.

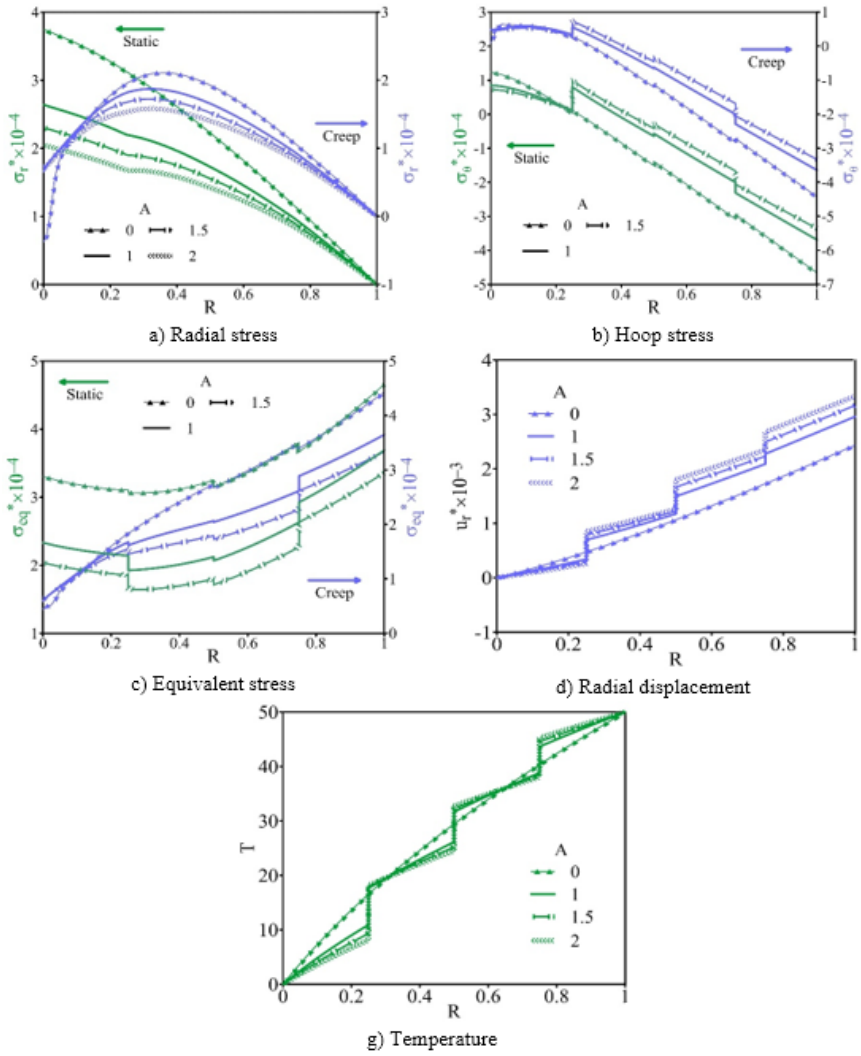


**Fig. 8.** Influence of imperfect bounding in both static and creep states $\gamma_1 = 0.02,\ \gamma_2 = 0.03,\ \gamma_3 = 0.04,\ \gamma_4 = 0.05$ . .

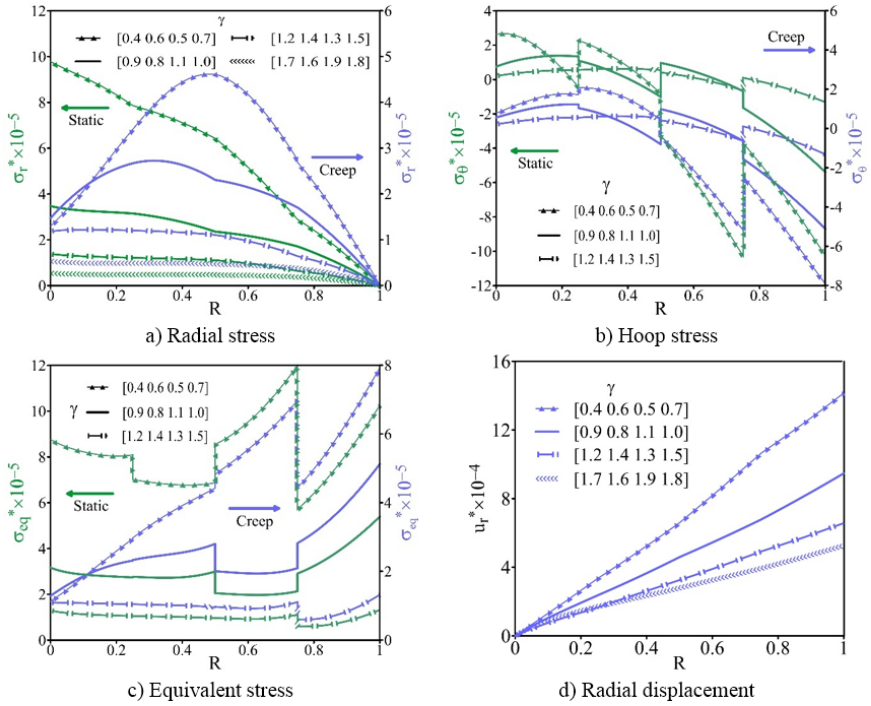


**Fig. 9.** Influence of grading index in both static and creep states.

### *4.6. Grading Index*

Fig. 9 highlights the effect of the grading index on the behavior of the multilayer FGM disc. The $dt = 2 \times 10^9$ considered as the analysis time. The maximum radial stress in both static and creep states occurs at the lowest grading index, while the minimum values correspond to the highest index. The maximum compressive hoop stress is concentrated at the outer layer, but the maximum tensile hoop stress is found near the inner layer when the layers are given the lowest grading index. In contrast, assigning a high grading index results in a more uniform hoop stress distribution and reduced interlayer jumps. The equivalent stress increases with a lower grading index, whereas higher values lead to a reduction. As seen, a higher grading index is required to decrease the radial displacement. Overall, the results indicate that appropriate selection of the grading index for each layer allows effective control of stress and displacement fields under both static and creep conditions.

## 5. Conclusion

Considering imperfect interlayer bonding, this paper presents a detailed analytical investigation of the time-dependent creep behavior of a functionally graded multi-layered rotating disc with variable thickness, subjected to hygrothermal and axial magnetic field loadings. The redistribution of stresses and radial displacement over time was evaluated using Prandtl–Reuss relations and Norton's creep law. The following conclusions can be listed based on the numerical results:

1. During creep evolution, radial, hoop, and equivalent stresses decrease across all layers, while radial displacement increases. The locations of peak radial and equivalent stresses shift outward over time.

2. Increasing angular velocity leads to elevated radial and equivalent stresses, as well as higher radial displacement. The position of maximum hoop and equivalent stresses transitions from the outer layer toward intermediate layers with increased angular velocity.

3. Axial magnetic fields amplify radial and hoop stresses, equivalent stress, and radial displacement. The tensile hoop stress at the inner radius becomes more pronounced under stronger magnetic fields, increasing the risk of crack initiation and growth.

4. Higher hygrothermal loads intensify all stress components and radial displacement. Particularly, the tensile hoop stress at the inner surface and the interlayer stress jumps rise significantly, which are critical due to the brittle nature of FGM materials.

5. The presence of bonding imperfections reduces stress magnitudes and radial displacement. The effects and interlayer jumps become more prominent with increasing imperfection coefficients,

also affecting temperature and moisture gradients.

6. The grading index has a critical influence on the stress and displacement distributions. Lower grading indices lead to higher stresses and larger displacements, while higher indices promote uniform stress profiles and reduce interlayer jumps.

## References


[1] M. Saadatfar, M. A. Babazadeh, M. Babaelahi, Effect of Convection, Internal Heat Source, and Solar Radiation on the Stress Analysis of a Rotating Functionally Graded Smart Disk. Iranian Journal of Science and Technology, J. Trans. Mech. Eng., 48(3) (2024) 1041-1061.

[2] M. Saadatfar, M. A. Babazadeh, M. Babaelahi, Creep analysis in a rotating variable thickness functionally graded disc with convection heat transfer and heat source, Mech. Time-Depend. Mater., 28(1) (2024) 19-41.

[3] K. Khanna, V. K. Gupta, S. P. Nigam, Modelling and analysis of creep in a variable thickness rotating FGM disc using Tresca and von Mises criteria. Iranian Journal of Science and Technology, Trans. Mech. Eng., 41(2) (2017) 109-119.

[4] M. Bayat, B. Sahari, M. Saleem, E. dezvareh, A. Mohazzab, Analysis of functionally graded rotating disks with parabolic concave thickness applying an exponential function and the Mori-Tanaka scheme, In IOP Conference Series: Materials Science and Engineering (Vol. 17, No. 1, p. 012005). IOP Publishing, (2011, February).

[5] S. Mert Kutsal and S.B. Cokun, Analysis of functionally graded rotating disks via analytical approximation methods, Mech. Based Des. Struct. Mach., 52(9) (2024) 6348-6367.

[6] M. Saadatfar, M. H. Zarandi, . Deformations and stresses of an exponentially graded magneto-electro-elastic non-uniform thickness annular plate which rotates with variable angular speed, Int. J. Appl. Mech., 12(05) (2020) 2050050.

[7] M. Saadatfar and M. Aghaie-Khafri, Hygrothermal analysis of a rotating smart exponentially graded cylindrical shell with imperfect bonding supported by an elastic foundation, Aerosp. Sci. Technol, 43 (2015) 37-50.

[8] P. K. Karimi Zeverdejani and Y. Kiani, Radially symmetric response of an FGM spherical pressure vessel under thermal shock using the thermally nonlinear Lord-Shulman model, Int. J. Press. Vessels Pip., 182 (2020) 104065.

[9] A. Ganczarski and D. Szubartowski, Plane stress state of FGM thick plate under thermal loading, Arch. Appl. Mech., 86(1) (2016) 111-120.

[10] M. Saadatfar and M. Aghaie-Khafri, Electromagnetothermoelastic behavior of a rotating imperfect hybrid functionally graded hollow cylinder, Smart Struct. Syst., 15(6) (2015) 1411-1437.

[11] M. Saadatfar and M. Aghaie-Khafri, Thermoelastic analysis of a rotating functionally graded cylindrical shell with functionally graded sensor and actuator layers on an elastic foundation placed in a constant magnetic field, J. Intell. Mater. Syst. Struct., 27(4) (2016) 512-527.

[12] M. Saadatfar and M. Aghaie-Khafri, On the behavior of a rotating functionally graded hybrid cylindrical shell with imperfect bonding subjected to hygrothermal condition, J. Therm. Stresses, 38(8) (2015) 854-881.

[13] M. Saadatfar, Effect of multiphysics conditions on the behavior of an exponentially graded smart cylindrical shell with imperfect bonding, Meccanica, 50(8) (2015) 2135-2152.

[14] H. Yaghoobi, A. Fereidoon, M. Khaksari Nouri, S. Mareishi, Thermal buckling analysis of piezoelectric functionally graded plates with temperature-dependent properties, Mech. Adv. Mater. Struct., 22(10) (2015) 864-875.

[15] M. Arefi, E.M.-R. Bidgoli, R. Dimitri, M. Bacciocchi, F. Tornabene, Application of sinusoidal shear deformation theory and physical neutral surface to analysis of functionally graded piezoelectric plate, Compos. B: Eng., 151 (2018) 35-50.

[16] A. M. Zenkour, Bending analysis of piezoelectric exponentially graded fiber-reinforced composite cylinders in hygrothermal environments, J. Mech. Mater. Des., 13(4) (2017) 515-529.

[17] P. Kumar, S. P. Harsha, Vibration response analysis of exponential functionally graded piezoelectric (EFGP) plate subjected to thermo-electro-mechanical load, Compos. Struct., 267 (2021) 113901.

[18] R. Singh, R. K. Saxena, K. Khanna, V. K. Gupta, Finite element modeling to analyze creep behavior of functionally graded rotating discs with exponential reinforcement and thickness profiles, Arch. Appl. Mech., 94(7) (2024) 2039-2058.

[19] M. Sahni, P. D. Mehta, R. Sahni, E. León-Castro, L. F. Espinoza-Audelo, Secondary creep analysis of FG rotating cylinder with exponential, linear and quadratic volume reinforcement, Materials, 15(5) (2022) 1803.

[20] F. Abdolkhani, M. Hashemian, F. Aghadavoudi, N. Habibi, Creep of autofrettaged thick-walled FGM cylindrical vessel. Proceedings of the Institution of Mechanical Engineers, J. Mech. Eng. Sci., 238(6) (2024) 2308-2328.

[21] V. K. Gupta, H. N. Chandrawat, S. B. Singh, S. Ray, Creep behavior of a rotating functionally graded composite disc operating under thermal gradient, Metall. Mater. Trans. A, 35(4) (2004) 1381-1391.

[22] V. K. Gupta, S. B. Singh, H. N. Chandrawat, S. Ray, Steady state creep and material parameters in a rotating disc of AlSiCP composite, Eur. J. Mech. A/Solids., 23(2) (2004) 335-344.

[23] D. Dharmpal, G. Manish, and V. K. Gupta, Creep behavior of rotating FGM disc with linear and hyperbolic thickness profiles, Kragujevac J. Sci., 37 (2015) 35-48.

[24] D. Deepak, V. K. Gupta, A. K. Dham, Creep modeling in functionally graded rotating disc of variable thickness, J. Mech. Sci. Technol., 24(11) (2010) 2221-2232.

[25] M. Rattan, T. Bose, N. Chamoli, S. B. Singh, Creep analysis of anisotropic functionally graded rotating disc subject to thermal gradation, In Materials Physics and Chemistry (pp. 71-88), (2020). Apple Academic Press.

[26] M. Shariyat, M. Ghafourinam, Hygrothermomechanical creep and stress redistribution analysis of thick-walled FGM spheres with temperature and moisture dependent material properties and inelastic radius changes, Int. J. Press. Vessels Pip., 169 (2019) 94-114.

[27] S. H. Kordkheili, M. Livani, Thermoelastic creep analysis of a functionally graded various thickness rotating disk with temperature-dependent material properties, Int. J. Press. Vessels Pip., 111 (2013) 63-74.

[28] D. Dharmpal, G. Manish, V. Gupta, Creep behavior of rotating FGM disc with linear and hyperbolic thickness profiles, Kragujevac J. Sci, 37 (2015) 35-48.

[29] S. Golmakaniyoon, F. Akhlaghi, Time-dependent creep behavior of AlSiC functionally graded beams under in-plane thermal loading, Comput. Mater. Sci., 121 (2016) 182-190.

[30] V. Gupta, S. B. Singh, Mathematical modeling of creep in a functionally graded rotating disc with varying thickness, Regen. Eng. Transl. Med., 2(3) (2016) 126-140.

[31] T. Bose, M. Rattan, Effect of thermal gradation on steady state creep of functionally graded rotating disc, Eur. J. Mech. A/Solids., 67 (2018) 169-176.

[32] A. Loghman, M. Abdollahian, A. Jafarzadeh Jazi, A.G. Arani, . Semi-analytical solution for electromagnetothermoelastic creep response of functionally graded piezoelectric rotating disk, Int. J. Therm. Sci., 65 (2013) 254-266.

[33] M. Saadatfar, M A. Babazadeh, and M. Babaelahi, . Creep analysis in a rotating variable thickness functionally graded disc with convection heat transfer and heat source, Mech. Time-Depend. Mater., 28(1) (2024) 19-41.

[34] M. Saadatfar, M. A. Babazadeh, M. Babaelahi, Thermoelastic creep evolution in a variable thickness functionally graded piezoelectric rotating annular plate considering convection and radiation heat transfer, Mech. Based Des. Struct. Mach., 52(8) (2024) 5944-5969.

[35] H. Zharfi, Creep relaxation in FGM rotating disc with nonlinear axisymmetric distribution of heterogeneity, Theor. Appl. Mech. Lett., 9(6) (2019) 382-390.

[36] V. Daghigh, H. Edalati, H. Daghigh, D. M. Belk, K. Nikbin, Time-dependent creep analysis of ultra-high-temperature functionally graded rotating disks of variable thickness, Forces in Mech., 13 (2023) 100235.

[37] H. M. A. Abdalla, D. Casagrande, L. Moro, Thermo-mechanical analysis and optimization of functionally graded rotating disks, J. Strain Anal. Eng. Des., 55(5-6) (2020) 159-171.

[38] Ö. C. Farukoğlu, İ, Korkut, Failure stress response of rotating multilayered fiber reinforced annular disk, Mech. Based Des. Struct. Mach., 51(9) (2023) 5164-5178.

[39] A. H. Akbarzadeh, D. Pasini, Multiphysics of Multilayered and Functionally Graded Cylinders Under Prescribed Hygrothermomagnetoelectromechanical Loading,J. Appl. Mech., 81(4) (2014) 041018.

[40] Y. Suo, H. Cui, B. Mei, D. Li, Y. Jiang, H. Sun, L. Zhang, . Finite element analysis on thermoelastic instability of multidisc clutches involving deformation modes of multilayer material friction disc, J. Tribol., 146(4) (2024) 044601.

[41] P. S. Ghatage, V. R. Kar, P. E. Sudhagar, On the numerical modelling and analysis of multi-directional functionally graded composite structures: A review, Compos. Struct., 236 (2020)111837.

[42] H. M. Wang, Dynamic electromechanical behavior of a triple-layer piezoelectric composite cylinder with imperfect interfaces, Appl. Math. Model., 35(4) (2011) 1765-1781.

[43] Y. D. Li and K. Y. Lee, Interaction between an electrically permeable crack and the imperfect interface in a functionally graded piezoelectric sensor, Int. J. Eng. Sci., 47(3) (2009) 363-371.

[44] D. Guinovart-Sanjuán, R. Rizzoni, R. Rodríguez-Ramos, R. Guinovart-Díaz, J. Bravo-Castillero, R. Alfonso-Rodríguez, F. Lebon, S. Dumont, I. Sevostianov, F. J. Sabina, Behavior of laminated shell composite with imperfect contact between the layers, Compos. Struct., 176 (2017) 539-546.

[45] H. T. Wang, J. H. Guo, X. Jiang, M. Z. Gao, Bending and vibration of one-dimensional hexagonal quasicrystal layered plates with imperfect interface, Acta Mech., 233(10) (2022) 4029-4046.

[46] M. Shaat, X. L. Gao, K. Li, A. G. Littlefield, . New analytical model for thermomechanical responses of multi-layered structures with imperfect interfaces, Acta Mech., 234(11) (2023) 5779-5818.

[47] W. J. Chang, Transient hygrothermal responses in a solid cylinder by linear theory of coupled heat and moisture, Appl. Math. Model., 18(8) (1994) 467-473.

[48] T. Dai, H. L. Dai, Analysis of a rotating FG-MEE circular disk with variable thickness under thermal environmentm, Appl. Math. Model., 45 (2017) 900-924.

[49] M. Bayat, M. Rahimi, M. Saleem, A. H. Mohazzab, I. Wudtke, H. Talebi, One-dimensional analysis for magneto-thermo-mechanical response in a functionally graded annular variable-thickness rotating disk, Appl. Math. Model., 38(19-20) (2014) 4625-4639.

[50] S. Kapuria, G. G. S. Achary, Exact 3D piezoelasticity solution of hybrid crossply plates with damping under harmonic electro-mechanical loads, J. Sound Vib., 282(3-5), 617-634. (2005).

[51] A. H. Akbarzadeh, Magnetoelectroelastic behavior of rotating cylinders resting on an elastic foundation under hygrothermal loading, Smart Mater. Struct., 21(12) (2012) 125013.

[52] H. L. Dai, H. J. Jiang, L. Yang, Time-dependent behaviors of a FGPM hollow sphere under the coupling of multi-fields, Solid State Sci., 14(5) (2012) 587-597.

[53] M. Saadatfar, Multiphysical time-dependent creep response of FGMEE hollow cylinder in thermal and humid environment, Mech. Time-Depend. Mater., 25(2) (2021) 151-173.

[54] T. Dai, H. L. Dai, Thermo-elastic analysis of a functionally graded rotating hollow circular disk with variable thickness and angular speedAppl. Math. Model., 40(17-18) (2016) 7689-7707.